



**HAL**  
open science

## **Dynamic Adsorption of CO<sub>2</sub> by CHA Zeolites -Size Matters**

Edwin Clatworthy, Sajjad Ghojavand, Rémy Guillet-Nicolas, Jean-Pierre Gilson,  
Philip Llewellyn, Nikolai Nesterenko, Svetlana Mintova

### ► **To cite this version:**

Edwin Clatworthy, Sajjad Ghojavand, Rémy Guillet-Nicolas, Jean-Pierre Gilson, Philip Llewellyn, et al.. Dynamic Adsorption of CO<sub>2</sub> by CHA Zeolites -Size Matters. Chemical Engineering Journal, 2023, 471, pp.144557. <10.1016/j.cej.2023.144557>. <hal-04283464>

**HAL Id: hal-04283464**

**<https://hal.science/hal-04283464v1>**

Submitted on 13 Nov 2023

**HAL** is a multi-disciplinary open access archive for the deposit and dissemination of scientific research documents, whether they are published or not. The documents may come from teaching and research institutions in France or abroad, or from public or private research centers.

L'archive ouverte pluridisciplinaire **HAL**, est destinée au dépôt et à la diffusion de documents scientifiques de niveau recherche, publiés ou non, émanant des établissements d'enseignement et de recherche français ou étrangers, des laboratoires publics ou privés.



HAL Authorization

# 1 Dynamic Adsorption of CO<sub>2</sub> by CHA Zeolites –

## 2 Size Matters

3 *Edwin B. Clatworthy,<sup>†\*</sup> Sajjad Ghossein,<sup>†</sup> Rémy Guillet-Nicolas,<sup>†</sup> Jean-Pierre Gilson,<sup>†</sup>*  
4 *Philip L. Llewellyn,<sup>‡</sup> Nikolai Nesterenko,<sup>‡</sup> Svetlana Mintova<sup>†\*</sup>*

5  
6 <sup>†</sup> Normandie Université, ENSICAEN, UNICAEN, CNRS, Laboratoire Catalyse et  
7 Spectrochimie (LCS), 14050 Caen, France

8 <sup>‡</sup> TotalEnergies OneTech, Centre Scientifique et Technique Jean Féger, Pau, France

9 <sup>‡</sup> TotalEnergies OneTech Belgium, Feluy, B-7181 Seneffe, Belgium

10

11 **ABSTRACT** The performance of K-CHA nanozeolite composed of discrete nanoparticles  
12 prepared by an organic template-free direct synthesis is compared to that of conventional  
13 micron-sized K-CHA with an order of magnitude difference in particle size and identical  
14 chemical composition (Si/Al ratio and cations) for the separation of dilute CO<sub>2</sub> from N<sub>2</sub>.  
15 Breakthrough curve analysis of the zeolites meshed to identical sizes demonstrates the  
16 superior performance of nanozeolites for gas separation due to the significantly faster  
17 diffusion of CO<sub>2</sub> molecules through the bed composed of meshed nanozeolite particles  
18 evidenced by the enhanced mass transfer, more rapid establishment of equilibrium, and faster  
19 desorption of CO<sub>2</sub>. Modelling of the CO<sub>2</sub> breakthrough curves indicates enhanced mass  
20 transfer properties of the CHA nanozeolite due to the higher linear driving force parameter  
21 values. Variation of the modelling parameters and back-calculation of the diffusion  
22 coefficients indicates that axial diffusion contributes significantly to the mass transfer  
23 behaviour yet also reveals significantly lower micropore diffusion resistance for the nano-  
24 sized K-CHA. These results demonstrate for rapid kinetically controlled sorption-based

25 separations, that by reducing the size of the discrete crystallites of the meshed adsorbent  
 26 particle by an order of magnitude, significant improvements in the utilization of the bed can  
 27 be achieved due to the shortening of the mass-transfer zone, improving the separation  
 28 performance.

29 **Keywords:** zeolites, crystal size, CO<sub>2</sub> adsorption, separation, breakthrough analysis

30 **Nomenclature**

$c_{in}$	concentration at column inlet, mol·m <sup>-3</sup>
$c_{out}$	concentration at column outlet, mol·m <sup>-3</sup>
$c_{g,i}$	component concentration in the gas phase, mol·kg <sup>-1</sup>
$c_{pg}$	specific heat capacity of gas at constant pressure, J·kg <sup>-1</sup> ·K <sup>-1</sup>
$c_{ps}$	specific heat capacity of adsorbent at constant pressure, J·kg <sup>-1</sup> ·K <sup>-1</sup>
$c_{pw}$	specific heat capacity of wall at constant pressure, J·kg <sup>-1</sup> ·K <sup>-1</sup>
$D_{ax}$	axial mass dispersion coefficient, m <sup>2</sup> ·s <sup>-1</sup>
$D_c$	micropore diffusivity, m <sup>2</sup> ·s <sup>-1</sup>
$D_p$	macropore diffusivity, m <sup>2</sup> ·s <sup>-1</sup>
$d_i$	internal diameter of column, m
$K$	dimensionless Henry's Law equilibrium constant
$K_i$	affinity constant
$K_{i,0}$	affinity constant at reference temperature
$k_f$	film mass transfer coefficient, s <sup>-1</sup>
$k_i$	overall mass transfer coefficient, s <sup>-1</sup>
$k_{in}$	heat transfer coefficient between the bed and wall, W·m <sup>-2</sup> ·K <sup>-1</sup>
$k_{out}$	heat transfer coefficient between the wall and bath, W·m <sup>-2</sup> ·K <sup>-1</sup>
$k_{LDF}$	effective mass transfer coefficient, s <sup>-1</sup>
$n_{adsorbed}$	amount of molecules adsorbed, mol
$q_{eq}$	adsorbed concentration in equilibrium with $c_{g,i}$ , mol·kg <sup>-1</sup>
$\bar{q}_i$	component average concentration on the adsorbed phase, mol·kg <sup>-1</sup>
$q_{max,i}$	maximal loading, mol·kg <sup>-1</sup>
$q_{max0,i}$	maximal loading at reference temperature $T_0$ , mol·kg <sup>-1</sup>
$R$	ideal gas constant, J·mol <sup>-1</sup> ·K <sup>-1</sup>
$r_c$	average crystal radius, m
$r_p$	average particle radius, m
$T$	bulk phase temperature, K
$T_0$	reference temperature for isotherm fitting
$T_w$	wall temperature, K
$T_{env}$	environmental temperature (reference temperature), K
$t$	Toth heterogeneity parameter
$t_0$	heterogeneity parameter at reference temperature $T_0$
$u$	interstitial velocity, m·s <sup>-1</sup>
$V_{He}$	volume of He, m <sup>-3</sup>

$V_{in}$	volume at column inlet, $m^{-3}$
$V_{out}$	volume at column outlet, $m^{-3}$
$WS$	wall thickness, m
$y_{adsorptive,i}$	adsorptive volume fraction
$\Delta H_{ads}$	isosteric enthalpy of adsorption, $J \cdot mol^{-1}$
$\Delta H_i$	isosteric enthalpy of adsorption for component $i$ , $J \cdot mol^{-1}$
$\alpha$	parameter for the temperature dependency of the Toth exponent
$\varepsilon$	bed porosity
$\varepsilon_p$	particle porosity
$\lambda$	axial heat dispersion coefficient, $J \cdot s^{-1} \cdot m^{-1} \cdot K^{-1}$
$\rho_p$	average particle density, $kg \cdot m^{-3}$
$\rho_b$	average fixed bed density, $kg \cdot m^{-3}$
$\rho_g$	fluid density, $kg \cdot m^{-3}$
$\rho_w$	wall density, $kg \cdot m^{-3}$
$\chi_i$	coefficient for the temperature dependency of the maximum capacity

31

## 32 Introduction

33 The bulk separation and purification of gases are essential industrial processes in which  
34 zeolites play key roles in a range of applications including gas drying, S removal, O<sub>2</sub> and N<sub>2</sub>  
35 production, landfill gas separation (CO<sub>2</sub>/CH<sub>4</sub>), and H<sub>2</sub> production from methane reforming  
36 and refinery off-gas.[1] In the last decade enormous efforts have been dedicated to  
37 developing materials for carbon capture and storage (CCS) because of the rising atmospheric  
38 concentration of CO<sub>2</sub> and its contribution to anthropogenic global climate change.[2-22]  
39 However, due to the presence of H<sub>2</sub>O in industrial streams, such as flue gas, the energy and  
40 cost efficient separation of CO<sub>2</sub> is considerably challenging. The high cationic content of  
41 industrial molecular sieves, such as 4A, 5A and 13X, and their strong interaction with H<sub>2</sub>O  
42 demands appropriate regeneration to maintain their longevity. Employment of activated  
43 alumina upstream of the molecular sieve can be also increase their lifetime considerably, but  
44 at additional capital cost.[23] While solvent-based absorption processes are currently the  
45 most widely applied for post-combustion CO<sub>2</sub> capture, these can be associated with large  
46 energy requirements for regeneration, degradation issues with temperature and the presence

47 of oxygen and toxicity.[24-26] With these points in mind, alternatives to the use of amines  
48 solvents such as green solvents, membranes and adsorption-based separations are  
49 investigated, with the latter of interest to the current study. Pressure swing adsorption (PSA)  
50 and temperature swing adsorption (TSA) are the processes often used for gas separation.  
51 Whilst PSA processes can be quite rapid (steps can occur in seconds), currently mature TSA  
52 process cycles can be quite long (hours). Whilst TSA may be quite adapted to anthropogenic  
53 CO<sub>2</sub> capture, shorter process sequences are required. A rapid TSA process is currently being  
54 developed,[27] where the whole capture, regeneration and conditioning steps can take a  
55 minute. In such cases however, kinetics of the gas/solid interactions are as important as the  
56 thermodynamics and to control the gas diffusion at the particle level can prove critical to  
57 separation properties.

58 The development of zeolite materials possessing high CO<sub>2</sub> separation performance has been a  
59 focal point because of the established roles zeolites play in petrochemistry and air separation  
60 processes thereby providing a rapidly deployable solution at an industrial scale.[23, 28]  
61 However, conventional zeolites are composed of micrometre sized particles which means a  
62 CO<sub>2</sub> molecule must diffuse a distance through the pores of a particle tens of thousands of  
63 times longer than its size. This problem can be partly addressed by improving molecular  
64 access to the zeolite micropores through introducing mesoporosity, or by reducing the  
65 particle size.[29, 30] However, while creating mesoporosity can significantly improve the  
66 diffusion and catalytic properties of zeolites, it typically involves either post-synthesis  
67 treatments or the use of expensive organic templates and structure directing agents,  
68 increasing the time, cost and waste of the material production.[31]

69 By preparing zeolites with nanoscale dimensions the distance guest molecules must diffuse  
70 through the particle can be reduced by an order of magnitude. To benefit from this we have  
71 developed pure inorganic one-pot syntheses of industrially important nanozeolites composed

72 of discrete nanoparticles.[32-38] While the yield of particular nanozeolite syntheses warrants  
73 further optimisation, the elimination of expensive organic structure-directing agents (OSDAs)  
74 and calcination treatments offers a reduction in energy consumption and emissions while also  
75 avoiding undesirable changes to the zeolite structure and properties caused by H<sub>2</sub>O vapour  
76 during calcination. Here we report on the comparison of K-CHA zeolites for the separation of  
77 CO<sub>2</sub> from a dilute stream at various temperatures, investigating the difference in performance  
78 by varying only the size of the discrete zeolite particles forming the meshed particles by an  
79 order of magnitude; the size of the meshed particles for both samples is identical. We provide  
80 direct experimental evidence and validation of the enhanced diffusion properties of adsorbent  
81 particles composed of discrete nano-sized zeolites applicable to industrially relevant  
82 separations. The concentration of CO<sub>2</sub> employed (5 vol%) is comparable to that of the  
83 exhaust of a natural gas combined-cycle plant.[39] The choice of examining high aluminium  
84 (Si/Al < 3) K-CHA zeolite derives from their attractive properties for CO<sub>2</sub> separation  
85 applications, *i.e.*, high CO<sub>2</sub> capacity, and selectivity towards CO<sub>2</sub> over N<sub>2</sub> (4 mmol/g, 27 with  
86 Si/Al = 2.4 and 2.1 mmol/g, 80 with Si/Al = 1.2).[6, 40, 41]

## 87 **Experimental**

### 88 **Materials**

89 All reagents were used as received unless otherwise specified. Potassium hydroxide (90  
90 wt%), LUDOX AS-40, sodium aluminate (NaAlO<sub>2</sub>, 40–45% Na<sub>2</sub>O, 50–56% Al<sub>2</sub>O<sub>3</sub>) and  
91 sodium hydroxide pellets (98 wt%) were purchased from Sigma-Aldrich. An aqueous  
92 solution of caesium hydroxide (CsOH, 50 wt% Cs) was prepared by dissolving caesium  
93 hydroxide (Alfa Aesar 20% H<sub>2</sub>O, 98%) in ultrapure (Type 1) water. Zeolite Y (H-form,  
94 CBV400), was purchased from Zeolyst. Ultrapure water was prepared by a Milli-Q Direct 8  
95 system and used for all syntheses. Quartz fine granular washed and calcined (900 °C, 0.2–0.8

96 mm, Merck) was used for blank breakthrough curve measurements. Helium (helium 4.5,  $\geq$   
97 99.995%), carbon dioxide (dioxyde de carbone 4.5,  $\geq$  99.995%) and nitrogen (azote 5.0,  $\geq$   
98 99.999%) were purchased from Linde.

## 99 **Synthesis**

100 Micron-sized K-CHA was prepared according to the procedure employed by Shang *et al.*[40]  
101 Zeolite Y powder (CBV400, 25 g) was added to de-ionised water (198 mL) and 9.5 M KOH  
102 solution (27 mL) in a sealed 250 mL polypropylene bottle. The mixture was shaken for 30 s  
103 and then placed in an oven preheated at 95 °C for 15 days. The sample was then cooled to  
104 room temperature and washed with de-ionised water by centrifugation at 20,000 rpm until the  
105 supernatant had a pH value between 7 and 8. The washed sample was then oven-dried at 60  
106 °C overnight. The yield of the micron-sized K-CHA based on the initial mass of CBV400  
107 was 37%.

108 Nano-sized K-CHA was prepared according to a procedure described previously.[42] 10.8 g  
109 of NaAlO<sub>2</sub> was mixed with 84.0 g of water with rapid stirring. Afterwards, 34.3 g of NaOH,  
110 16.5 g of KOH, and 8.8 g of CsOH (50 wt% Cs in water) were added and stirred for 2 h to  
111 obtain a clear solution. 200 g of LUDOX AS-40 was added dropwise under vigorous stirring  
112 to make a final composition of 0.284 Cs<sub>2</sub>O: 2.27 K<sub>2</sub>O: 8.56 Na<sub>2</sub>O: 22.9 SiO<sub>2</sub>: 1.00 Al<sub>2</sub>O<sub>3</sub>: 198  
113 H<sub>2</sub>O. The alkali colloidal gel was then aged under vigorous stirring at room temperature for  
114 17 days followed by hydrothermal treatment in a static oven at 90 °C for 7 h. The CHA  
115 nanocrystals were recovered by centrifugation and washed with hot water (90 °C) until a  
116 neutral pH (7–8) of the decanted solution was achieved. The recovered CHA nanocrystals  
117 were dried in an oven at 60 °C overnight. The final as-prepared CHA nanocrystals were ion  
118 exchanged with a 1 M KCl solution with a liquid/solid ratio (ml/g) of 40 for 2 hours.  
119 Afterwards, the CHA nanocrystals were recovered by centrifugation and washed with

120 deionised water three times. This procedure was repeated three times, and the recovered  
121 nano-sized K-CHA was dried in an oven at 60 °C overnight. The yield of the nano-sized K-  
122 CHA based on the initial combined mass of SiO<sub>2</sub> and Al<sub>2</sub>O<sub>3</sub> was 21%.

### 123 **Characterisation**

124 Powder X-ray diffraction (PXRD) patterns were collected with a PANalytical X'Pert Pro  
125 diffractometer using Cu-Kα<sub>1</sub> radiation ( $\lambda = 1.5406 \text{ \AA}$ , 45 kV, 40 mA). The patterns were  
126 collected between 5 and 60° 2 $\theta$  with a step size of  $\sim 0.0167^\circ$  and time per step of 1000 s.  
127 Elemental analysis was performed by inductively-coupled plasma mass spectrometry (ICP-  
128 MS) using a 7900 ICP-MS from Agilent Technologies. Samples (50 mg) were digested at  
129 110 °C for 1 h with hydrofluoric acid and aqua regia (6:1 vol. ratio) followed by  
130 neutralisation with boric acid (2 g) and de-ionised water (10 mL) and stirred overnight. The  
131 samples were then diluted up to 100 mL; a 10 mL aliquot was filtered before analysis.  
132 Thermogravimetric analysis (TG/DTG) was performed using a Setsys Evolution  
133 (SETARAM). Analysis under air was performed by heating from 30 to 800 °C (heating rate  
134 of 10 °C min<sup>-1</sup>) and held at 800 °C for 10 minutes. Scanning electron microscopy (SEM) of  
135 samples was performed using a Tescan Mira I LMH operating at 30 kV, samples were coated  
136 in metal before analysis. Particle size analysis was performed using ImageJ. Energy-  
137 dispersive X-ray spectroscopy (EDS) analysis of samples was performed using two Bruker  
138 XFLASH 6/30 detectors; the composition was determined from the average of several  
139 different measured points. Low temperature N<sub>2</sub> adsorption/desorption isotherms were  
140 measured at -196 °C using a Micromeritics 3Flex Surface Characterization unit. Samples  
141 were degassed at 350 °C (heating rate of 1 °C min<sup>-1</sup>) under vacuum for 8 h prior to analysis.  
142 High temperature (20, 40 and 60 °C) N<sub>2</sub> and CO<sub>2</sub> adsorption isotherms were measured on a  
143 Micromeritics ASAP 2020 instrument, samples were degassed at 350 °C (heating rate of 1 °C  
144 min<sup>-1</sup>) under vacuum for 8 h. CO<sub>2</sub> and N<sub>2</sub> isosteric enthalpies of adsorption ( $\Delta H_{\text{ads}}$ ) were

145 calculated directly from the experimental data points of the isotherms recorded at 20, 40 and  
146 60 °C using the Clausius Clapeyron equation in the VersaWin software. Mercury porosimetry  
147 was performed using a Micromeritics AutoPore V. *In situ* FTIR spectroscopic analysis was  
148 performed using a self-supported pellet (~20 mg, 16 mm diameter) of zeolite sample; the  
149 transmission spectra were recorded with a ThermoScientific Nicolet iS50 FTIR spectrometer  
150 equipped with an MCT detector, at a spectral resolution of 4 cm<sup>-1</sup>. An IR-cell equipped with  
151 a heating device was used to activate the samples at 350 °C prior to the measurements. The  
152 cell was connected to a high vacuum line of 10<sup>-6</sup> Torr. The sample was activated by heating  
153 with a ramp rate of 3 °C min<sup>-1</sup> followed by heating at 350 °C for 4 h under high vacuum. All  
154 spectra were recorded at room temperature and normalised to the area and mass of the pellet;  
155 determination of the physisorption and chemisorption isotherms was performed as described  
156 previously.[43]

### 157 **Breakthrough Curve Analysis**

158 Breakthrough curve experiments were performed using a 3P Instruments mixSorb SHP eco  
159 and Cirrus-3 Quadrupole Mass Spectrometer. Powder samples of zeolite adsorbent were  
160 initially pelletised by loading the powder between two core dice in a 20 mm die sleeve, with a  
161 base plate and plunger, and increasing the applied pressure to ~1.5 tonnes. The pellets were  
162 gently crushed with an agate pestle and meshed from 60 to 35 (250–500 µm) before being  
163 loaded into the column, weighed, and covered with a thin layer of glass wool. After each  
164 instance of loading the meshed sample into the column, the column was tapped 100 times to  
165 remove inter-particle voids. The inner diameter of the column was 6 mm and the height of the  
166 adsorbent bed was 6 cm. The ratio of the column inner diameter to the meshed particle  
167 diameter was 12–24. The samples were pre-treated under He flow (20 mL/min) with heating  
168 from room temperature to 300 °C at 10 °C/min (measured by an internal temperature probe)  
169 and held at 300 °C for 6 h using a heating mantle. TG analysis of the zeolite samples was

170 performed to determine the weight-loss of water during the pre-treatment step. The final  
171 amounts of nano-sized and micron-sized K-CHA loaded in the column after activation were  
172 0.601 and 0.676 g respectively. After pre-treatment the samples were kept under a flow of  
173 He (20 mL) at room temperature before commencing the breakthrough curve experiments.

174 Breakthrough curve experiments were conducted using a ternary mixture of CO<sub>2</sub>, N<sub>2</sub>  
175 (analytical components) and He (carrier gas) at 1 bar with a flowrate of 2, 10 and 28 mL/min  
176 respectively (total 40 mL/min), representing 5, 25 and 70 vol% of the feed composition for  
177 the adsorption step. Prior to the breakthrough curve experiments the mass spectrometer was  
178 calibrated by passing the ternary feed mixture through a bypass line to the mass spectrometer.  
179 Before contacting the ternary feed mixture with the adsorbent column the sample was  
180 maintained under He flow. The adsorption feed mixture was flowed through the adsorbent  
181 column after the temperature and spectrometer signals were stable, as determined using a  
182 bypass line. After a specified amount of time whereby the bed had reached equilibrium,  
183 desorption was conducted immediately by switching the feed to 100% He (40 mL/min). Both  
184 the adsorption and desorption steps for each experiment were conducted at the same  
185 temperature; experiments were conducted at 20, 40 and 60 °C by immersing the column in a  
186 water bath isothermally maintained by a chiller. The time for each step of the analysis was 60  
187 min at 20 °C and 30 min at 40 and 60 °C to allow sufficient time for the bed to reach  
188 equilibrium after breakthrough. The pressure drop across the column loaded with sample was  
189 determined by a pressure sensor located immediately before the column and the pressure  
190 controller located immediately after the column. For all experiments conducted the pressure  
191 drop was < 0.07 bar or 6% of the column pressure.

192 All breakthrough curve data was processed using the mixSorb Manager software. The  
193 differential loading of the adsorbates (CO<sub>2</sub> and N<sub>2</sub>) was calculated from the integrated areas  
194 exemplified in Figures S1 and S2.

195 
$$n_{\text{adsorbed}} = \int V_{\text{in}}(t)c_{\text{in}}(t)dt - \int V_{\text{out}}(t)c_{\text{out}}(t)dt \quad (1)$$

196 The advanced computed flowrate changes was employed to account for changes in the flow  
 197 rate using the He carrier gas as an internal standard.

198 
$$V_{\text{out}}(t) = \frac{V_{\text{He}}(t)}{1 - \sum_{i=1}^n y_{\text{adsorptive},i}(t)} \quad (2)$$

199 Blank experiments under identical feed composition, temperature, flowrate and pressure  
 200 conditions were performed using granular quartz to determine the loading of molecules in the  
 201 free space between the adsorbent particles and were directly subtracted from the loading  
 202 values of the zeolite samples (Fig. S3). He is considered as a non-adsorbing gas. The dead-  
 203 time of the system was estimated at  $\approx 2$  s based on the time of the activation of the mass-flow  
 204 controllers and the recording of the flow composition by the mass spectrometer through the  
 205 by-pass line. The void fraction or bed porosity was calculated using the dry mass of the  
 206 meshed K-CHA zeolite, the bulk particle density, and the internal column volume.

207 **Breakthrough Curve Modelling**

208 All isotherm and CO<sub>2</sub> breakthrough curve modelling was performed using the 3P-Sim  
 209 software package. The experimental CO<sub>2</sub> adsorption isotherms were fitted with a temperature  
 210 dependent model. Sips, Dual-Site Langmuir and Toth models were employed; Toth afforded  
 211 the best goodness of fit of the data and was employed for the CO<sub>2</sub> breakthrough curve  
 212 modelling. The parameters obtained from the modelling of the CO<sub>2</sub> adsorption isotherms with  
 213 the Toth equation (3) which were used in the CO<sub>2</sub> breakthrough curve modelling are  
 214 presented in Table S4.

215 
$$q_{eq} = q_{max,i} \cdot \frac{K_i \cdot c_{g,i}}{(1 + (K_i \cdot c_{g,i})^t)^{\frac{1}{t}}} \quad (3)$$

216 The temperature dependency of the isotherm parameters including the affinity constant,  $K_i$ ,  
217 maximum loading,  $q_{max}$ , and heterogeneity parameter,  $t$ , are accounted for with the following  
218 equations:

$$219 \quad K_i = K_0 \cdot \exp\left(\frac{\Delta H_{ads}}{R} \left(\frac{1}{T} - \frac{1}{T_0}\right)\right) \quad (4)$$

$$220 \quad q_{max,i} = q_{max,0} \cdot \exp\left(\chi_i \left(1 - \frac{T}{T_0}\right)\right) \quad (5)$$

$$221 \quad t = t_0 + \alpha \left(1 - \frac{T}{T_0}\right) \quad (6)$$

222 Global parameters for the CO<sub>2</sub> breakthrough curve modelling are presented in Table 1.  
223 Breakthrough curves were calculated with the following assumptions commonly employed in  
224 the literature:[44, 45]

- 225 1. Ideal gas behaviour of the adsorptive through the column.
- 226 2. No mass, heat or velocity gradients in the radial direction; instantaneous thermal  
227 equilibrium between the adsorbent and gas.
- 228 3. Dispersed plug flow model.
- 229 4. Negligible effects due to external mass transfer (film mass transfer and macropore  
230 diffusion).
- 231 5. Description of the mass transfer through the particle by the linear driving force (LDF)  
232 model.[46-48]
- 233 6. Heat capacity of the carrier gas dominates.
- 234 7. Heat capacity of the adsorbed phase neglected.
- 235 8. Constant internal (bed-wall) and external (wall-bath) heat transfer, and axial heat  
236 dispersion.
- 237 9. Constant and uniform adsorbent/bed porosity.

238 10. No pressure drop, constant pressure.

239 The model consists of dispersive plug flow with non-isothermal behaviour and variable gas  
240 velocity described by a mass and energy balance for the fixed bed and an energy balance for  
241 the column wall. The mass balance is expressed as:

$$242 \quad \frac{\partial c_{g,i}}{\partial t} = D_{ax} \frac{\partial^2 c_{g,i}}{\partial z^2} - u \frac{\partial c_{g,i}}{\partial z} - c_{g,i} \frac{\partial u}{\partial z} - \frac{(1-\varepsilon)}{\varepsilon} \rho_p \frac{\partial \bar{q}_i}{\partial t} \quad (7)$$

243 With respect to the assumptions employed for the calculations, the two energy balance  
244 equations are expressed as:

$$245 \quad \Delta H_i \rho_b (1 - \varepsilon) \frac{\partial \bar{q}_i}{\partial t} - (c_{ps} \cdot \rho_b (1 - \varepsilon) + c_{pg} \cdot \varepsilon \cdot \rho_g) \frac{\partial T}{\partial t} - u \varepsilon \rho_g c_{pg} \frac{\partial T}{\partial z} - T \varepsilon \rho_g c_{pg} \frac{\partial u}{\partial z} +$$
$$246 \quad \lambda \varepsilon \frac{\partial^2 T}{\partial z^2} - k_{in} \frac{4}{d_i} (T - T_w) = 0 \quad (8)$$

$$247 \quad k_{in} \cdot d_i (T - T_w) - (d_i \cdot WS + WS^2) c_{pw} \cdot \rho_w \frac{\partial T_w}{\partial t} - k_{out} (d_i + 2 \cdot WS) (T_w - T_{env}) = 0 \quad (9)$$

248 The heat transfer parameters,  $k_{in}$  (bed-wall) and  $k_{out}$  (wall-bath), and the axial heat dispersion  
249 ( $\lambda$ ) were estimated according to the according to the shape of the breakthrough curve. The  
250 axial dispersion coefficient was calculated using the correlation according to Kast in the 3P-  
251 Sim software package [47]:

$$252 \quad D_{ax} = u \cdot \frac{3 \cdot 10^{-3}}{2} \text{ for } 2r_p < 3 \text{ mm} \quad (10)$$

253 Neglecting the external mass transfer resistance and using the LDF approach, the mass  
254 transfer is expressed as[49]:

$$255 \quad \frac{\partial \bar{q}_i}{\partial t} = k_{LDF} (q_{eq} - \bar{q}_i) \quad (11)$$

256 The LDF parameter was assumed to be constant for a given operation and fitted to each  
257 breakthrough curve. Calculations were performed using the Crank-Nicolson solver (trapezoid

258 scheme). The bed porosity was calculated from the dry mass of zeolite and the bulk particle  
 259 density.

260

261

262 **Table 1.** Column, adsorbent and carrier gas parameters used for modelling the CO<sub>2</sub>  
 263 breakthrough curves of the nano- and micron-sized K-CHA.

Parameter	Value	Source	
<b>Column</b>			
Bed height (cm)	6	Measured	
Column inner diameter (cm)	0.6	Manufacturer	
Gas flow (mL·min <sup>-1</sup> )	40	Measured	
Column temperature (°C)	20, 40, 60	Measured	
Pressure (bar)	1.1	Measured	
Axial dispersion coefficient (m <sup>2</sup> ·s <sup>-1</sup> )	nano	micron	W. Kast estimation
	8.98×10 <sup>-5</sup>	6.97×10 <sup>-5</sup>	
	9.46×10 <sup>-5</sup>	7.40×10 <sup>-5</sup>	
	9.89×10 <sup>-5</sup>	7.92×10 <sup>-5</sup>	
Wall thickness (mm)	3	Manufacturer	
Wall density (g·cm <sup>-3</sup> )	7.9	Assumed, stainless steel	
Heat transfer bed-wall (internal), [W/(m <sup>2</sup> ·K)]	50	Estimated	
Heat transfer wall-bath (external), [W/(m <sup>2</sup> ·K)]	500	Estimated	
Heat capacity wall [J/(K·g)]	0.477	Assumed, stainless steel	
Axial heat dispersion [J/(K·min·cm)]	5	Estimated	
<b>Adsorbent</b>			
Mass (g)	0.601 (nano), 0.676 (micron)	Measured	
Particle diameter (mm)	0.25	Assumed	
Bed porosity	0.39 (nano), 0.49 (micron)	Measured	
Particle porosity	0.54 (nano), 0.49 (micron)	Measured	
Heat capacity [J/(K·g)]	1.27	Reference[50]	
<b>Carrier Gas</b>			
Molecular weight (g·mol <sup>-1</sup> )	4.0	NIST	
Heat capacity [J/(K·g)]	5.19	NIST	

264

265 Calculation of the MTZ was performed using equation (12):

266

$$267 \quad 1 - \left( \frac{\text{time to breakthrough} \left( \frac{C}{C_0} > 1 \times 10^{-4} \right), \text{min}}{\text{time of bed saturation} \left( \frac{C}{C_0} = 0.95 \right), \text{min}} \right) \times \text{bed length, cm} \quad (12)$$

268

269 Calculation of the CO<sub>2</sub>/N<sub>2</sub> selectivity for the competitive dynamic adsorption experiments  
270 was performed using equation (13):

$$271 \quad CO_2/N_2 \text{ Selectivity} = \left( \frac{q_{CO_2}}{n_{CO_2}} \right) / \left( \frac{q_{N_2}}{n_{N_2}} \right) \quad (13)$$

272 Where  $q$  is the differential loading of the adsorbate and  $n$  is the molar amount of adsorbate in  
273 the feed.

274

## 275 **Results and Discussion**

### 276 **Synthesis and Characterisation of K-CHA**

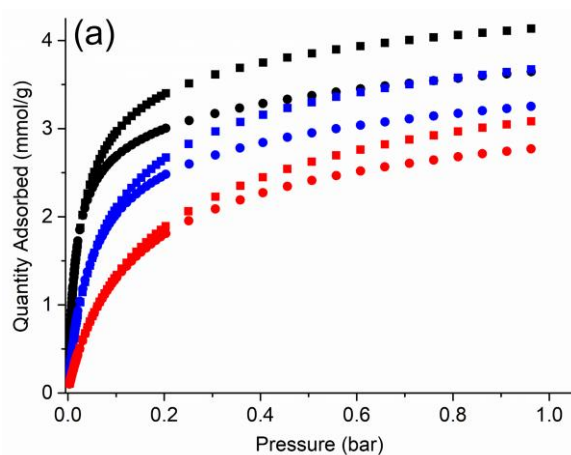
277 A conventional well-studied micron-sized K-CHA was prepared according to the patent  
278 literature of Bourgogne *et al.*[40, 51, 52] The nano-sized K-CHA was prepared following an  
279 up-scaled procedure derived from our previous work by Ghosvami *et al.* using an identical  
280 precursor composition, ageing time, and hydrothermal treatment.[42, 43] The synthesis of  
281 nano-sized chabazite has been methodically optimised to obtain discrete zeolite nano-  
282 crystallites of sizes below 100 nm with a specific Si/Al ratio. Both samples are highly  
283 crystalline (Fig. S4) with near-identical chemical compositions (Table S1); the XRD patterns  
284 of both samples are consistent with those previously reported for hydrated K-CHA.[53] The  
285 broad Bragg reflections of the nano-sized K-CHA are indicative of the presence of nano-  
286 sized crystalline domains.[42] The size of the crystalline domains was determined by  
287 Scherrer analysis as 80 nm for the nano-sized K-CHA and 200 nm for the micron-sized K-  
288 CHA. Thermogravimetric analysis of the nano- and micron-sized K-CHA samples reveals  
289 they possess a similar content of water of 17 and 19 wt% respectively (Fig. S5). Scanning  
290 electron microscopy (SEM) results confirms the order of magnitude difference in the particle  
291 size between the samples. Analysis of the nano-sized K-CHA shows the sample is composed  
292 of discrete nano-crystallites with primary particle sizes ranging predominantly between 50–  
293 80 nm (Figs S6a).[42] In comparison, the morphology of the micron-sized K-CHA is that of

294 irregular flake-like particles approximately 100–300 nm thick and 400–1000 nm at maximum  
295 width; the particles are composed of intergrown crystallite aggregates approximately 40–80  
296 nm in size (Figs S6b).[52]

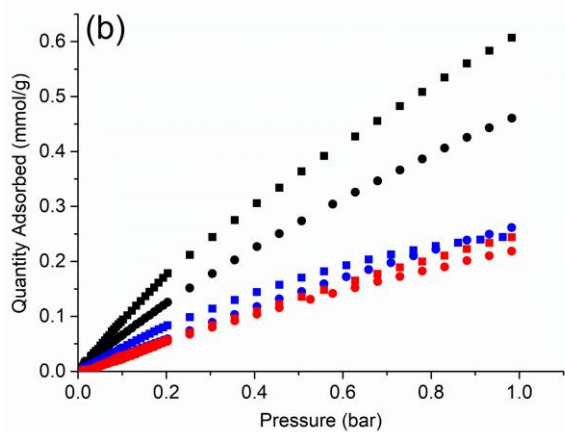
297 The difference in the textural properties of both samples is also evidenced by N<sub>2</sub> sorption  
298 analysis performed at –196 °C; both samples exhibit low micropore adsorption due to  
299 trapdoor behaviour which restricts access of N<sub>2</sub> to the micropores, however, the nano-sized  
300 K-CHA possesses significant inter-particle mesoporosity at high relative pressure due to its  
301 nanoparticle morphology (Fig. S7).[40] Both samples were subjected to single component  
302 CO<sub>2</sub> and N<sub>2</sub> sorption analysis at 20, 40 and 60 °C up to 1 bar (Figs 1 (a) and (b), Tables S2  
303 and S3). The CO<sub>2</sub> and N<sub>2</sub> adsorption capacity decreases with increasing temperature (Fig. 1);  
304 for both samples, the adsorbed amount of N<sub>2</sub> is low and increases linearly with increasing  
305 pressure while CO<sub>2</sub> exhibits a Type I isotherm due to strong adsorbent-adsorbate interactions.  
306 The slightly lower CO<sub>2</sub> adsorption capacity of the nano-sized K-CHA is due to the presence  
307 of a phillipsite impurity. The isosteric enthalpy of adsorption ( $\Delta H_{\text{ads}}$ ) as a function of loading  
308 were determined from the raw single-component isotherms (Fig. 1(c)). Both samples exhibit  
309 near-homogeneous adsorption sites for CO<sub>2</sub>; the  $\Delta H_{\text{ads}}$  of the nano-sized K-CHA decreases  
310 above a coverage of 2 mmol/g due to the saturation of the dual-cation adsorption sites and  
311 limited inter-molecular interactions.[35, 43, 54, 55] Both samples also exhibit similar trends  
312 for the N<sub>2</sub>  $\Delta H_{\text{ads}}$  with a minor decrease as the loading increases, however, the decrease is  
313 more significant for the nano-sized K-CHA. The lower N<sub>2</sub>  $\Delta H_{\text{ads}}$  of the nano-sized K-CHA is  
314 ascribed to the higher external surface of the particles providing lower energy adsorption  
315 sites. Temperature-dependent modelling of the CO<sub>2</sub> adsorption isotherms was performed  
316 using the Sips, Dual-Site Langmuir and Toth equations. The Toth model afforded the best  
317 goodness of fit of the data (Fig. S8) and the parameters obtained were used for the modelling  
318 of the CO<sub>2</sub> breakthrough curves (Table S4). Satisfactory temperature-dependent models of

319 the N<sub>2</sub> adsorption isotherms could not be obtained ( $R^2 < 0.990$ ) and so the IAST selectivity  
320 was not determined.

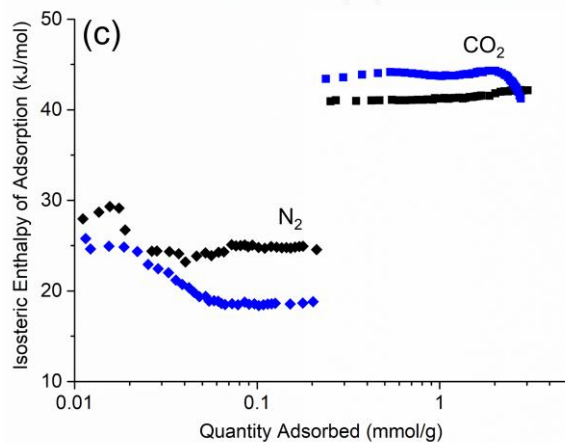
321



322



323

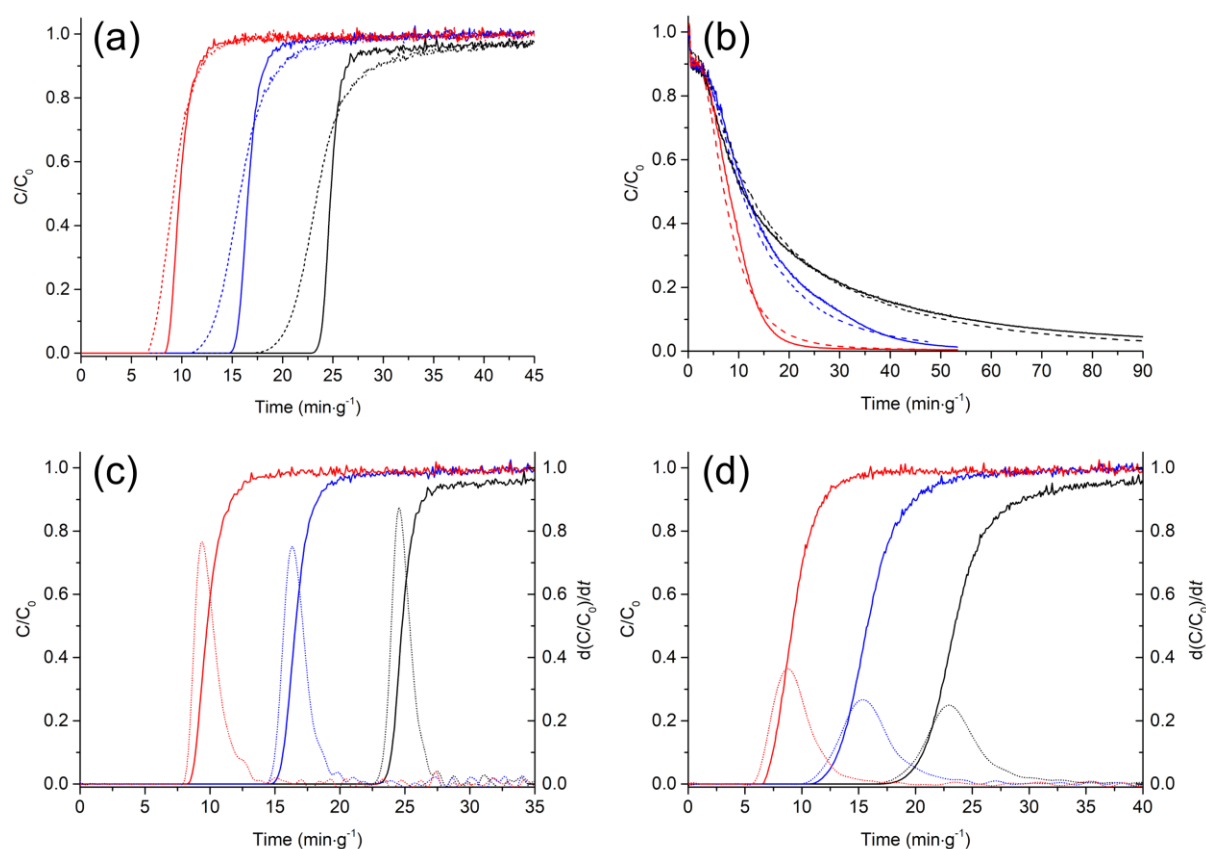


324 **Figure 1.** (a) CO<sub>2</sub> and (b) N<sub>2</sub> adsorption isotherms recorded at 20 (black), 40 (blue) and 60  
325 °C (red) on nano-sized (circles) and micron-sized (squares) K-CHA. (c) CO<sub>2</sub> (squares) and  
326 N<sub>2</sub> (diamonds) isosteric enthalpies of adsorption for nano-sized (blue) and micron-sized  
327 (black) K-CHA.  
328

## 329 **Dynamic Adsorption of CO<sub>2</sub>/N<sub>2</sub> on K-CHA and Breakthrough Curve Modelling**

330 Breakthrough curve analysis of the K-CHA samples was conducted using a ternary mixture  
331 of He/N<sub>2</sub>/CO<sub>2</sub> (70/25/5 vol%) at 1 bar and 20, 40 and 60 °C (Fig. 2); plots of the entire  
332 adsorption step show the breakthrough of N<sub>2</sub> on the K-CHA samples is instantaneous and  
333 exhibits a roll-up feature due to the displacement of N<sub>2</sub> by CO<sub>2</sub> from within the bed (Fig. S9).  
334 Due to the difference of the mass between the adsorbent, column and water bath the  
335 temperature profile of the column did not change significantly during the breakthrough  
336 experiment (Figure S10, Table S5). A minor temperature excursion of 0.30 and 0.25 °C was  
337 observed for the micron- and nano-sized K-CHA for the breakthrough curve analyses at 20  
338 °C; smaller deviations were observed at 40 °C, and no discernible temperature excursion was  
339 observed at 60 °C. The CO<sub>2</sub> breakthrough profiles of the K-CHA samples clearly exhibit  
340 significantly steeper curves for the nano-sized K-CHA across the measured temperatures  
341 compared to the micron-sized sample (Fig. 2a), indicative of more uniform diffusion of CO<sub>2</sub>  
342 through the bed and a reduction in the length of the MTZ, *i.e.* enhanced overall kinetics.  
343 While both K-CHA samples were prepared with the same mesh, the discrete nano-crystallites  
344 of the nano-sized K-CHA facilitate significantly more rapid intraparticle diffusion. This is  
345 also visualised by the plots of  $d(C/C_0)/dt$  illustrating the higher rate of change of the slope of  
346 the breakthrough curve for the nano-sized K-CHA compared to the micron-sized K-CHA  
347 (Figs 2c and d). A slight decrease in the slope of the breakthrough curve for nano-sized K-  
348 CHA occurs when the temperature increases from 20 to 40 °C, while the micron-sized K-  
349 CHA exhibits a slight increase in the breakthrough curve slope above 40 °C. The time  
350 necessary to achieve the desorption under pure He flow (Fig 2b) of CO<sub>2</sub> ( $C/C_0 < 0.05$ )  
351 dramatically decreased with increasing temperature for both samples; at 60 °C the nano- and  
352 micron-sized K-CHA required 11 and 14 minutes respectively. The difference in the  
353 desorption behaviour between the samples is not as dramatic as the initial breakthrough

354 because of the endothermic nature of the desorption step. Increasing the bed temperature  
 355 from 20 to 60 °C resulted in a linear decrease of the differential loading of CO<sub>2</sub> at saturation  
 356 for both K-CHA samples (Table 2). The differential loadings of CO<sub>2</sub> calculated from the  
 357 competitive breakthrough curves compare well with the isotherm values. In comparison, the  
 358 integration of the N<sub>2</sub> loading from the breakthrough curves affords values five times higher  
 359 compared to the equilibrium isotherms. Alternatively, integration under the N<sub>2</sub> desorption  
 360 curves was performed to calculate the N<sub>2</sub> loading, affording realistic values comparable to  
 361 earlier work by Du *et al.*[56] Overall, both samples exhibit similar selectivity towards CO<sub>2</sub>  
 362 over N<sub>2</sub>; the nano-sized K-CHA exhibits slightly higher CO<sub>2</sub> loading under dynamic  
 363 adsorption conditions.



364  
 365 **Figure 2.** CO<sub>2</sub> breakthrough and desorption curves, and first derivatives of CO<sub>2</sub> breakthrough  
 366 curves at 20 °C (black), 40 °C (blue) and 60 °C (red) obtained from competitive dynamic  
 367 adsorption experiments, He/N<sub>2</sub>/CO<sub>2</sub>, 70/25/5. (a) CO<sub>2</sub> breakthrough curves and (b) CO<sub>2</sub>  
 368 desorption curves of the nano-sized (solid) and micron-sized (dashed) K-CHA zeolites. CO<sub>2</sub>  
 369 breakthrough curves (solid) and first derivative (dashed) of the (c) nano-sized and (d)  
 370 micron-sized K-CHA zeolites.

371 **Table 2.** Differential loading of CO<sub>2</sub> calculated from breakthrough curves at saturation, N<sub>2</sub>  
 372 differential loading calculated from desorption curves, and CO<sub>2</sub>/N<sub>2</sub> selectivity calculated  
 373 from equation 13. Data from breakthrough curve analysis (He/N<sub>2</sub>/CO<sub>2</sub>, 70/25/5) at 20, 40 and  
 374 60 °C.

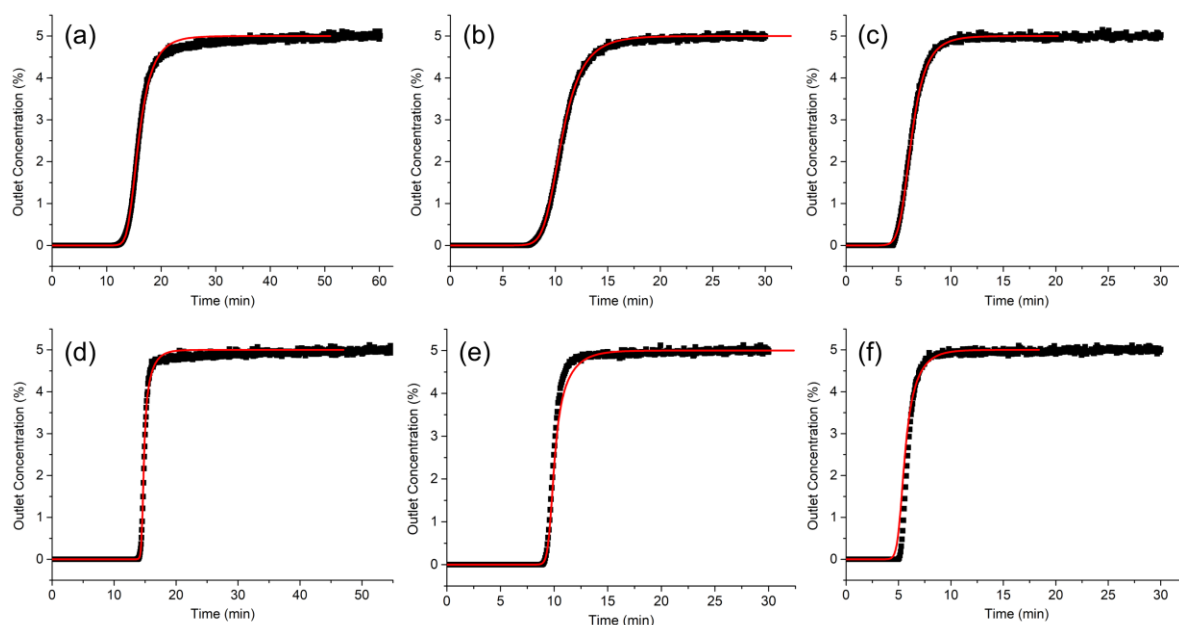
Temperature (°C)	Nano-sized K-CHA			Micron-sized K-CHA		
	Differential loading, q (mmol/g)		CO <sub>2</sub> /N <sub>2</sub> selectivity	Differential loading, q (mmol/g)		CO <sub>2</sub> /N <sub>2</sub> selectivity
	CO <sub>2</sub>	N <sub>2</sub>		CO <sub>2</sub>	N <sub>2</sub>	
20	2.33	0.085	137	2.22	0.092	121
40	1.49	0.041	182	1.43	0.070	102
60	0.87	0.007	618	0.82	0.006	685

375

376 Comparison of the CO<sub>2</sub> breakthrough curves of the nano- and micron-sized K-CHA at 60 °C,  
 377 akin to flue gas conditions, further highlights the difference in the performance of the solid  
 378 adsorbents with different particle sizes (Fig. S11). By defining the MTZ between the first  
 379 point of breakthrough,  $C/C_0 > 1 \times 10^{-4}$  (*i.e.* the end of pure production of the weakly adsorbing  
 380 component), and saturation of the bed,  $C/C_0 = 0.95$ , it is clear that the micron-sized K-CHA  
 381 not only exhibits a shallower breakthrough curve but also takes a longer time to reach  
 382 equilibrium. Due to the similar CO<sub>2</sub> uptakes of 0.87 mmol/g for both K-CHA samples at 0.05  
 383 bar (*i.e.* the partial pressure of CO<sub>2</sub> in the feed) at 60 °C, the longer time to reach equilibrium  
 384 for the micron-sized K-CHA is ascribed to the larger particle size and thus longer diffusion  
 385 path length. Expressed as a percentage of the total bed length, the length of the MTZ is  
 386 significantly shorter (35% vs 52%) for the nano- compared to the micron-sized K-CHA  
 387 (Table S6).

388 In addition, simple modelling of the CO<sub>2</sub> breakthrough curves was performed to extract the  
 389 effective mass transfer coefficient, or linear driving force parameter ( $k_{LDF}$ ), to describe the  
 390 mass transfer kinetics of CO<sub>2</sub> through the adsorbent bed (Fig. 3).[44] Thus a global  
 391 characteristic of the diffusion can be compared between the two samples. Employing the  
 392 parameters derived from the Toth models of the CO<sub>2</sub> adsorption isotherms at different  
 393 temperatures, the fitted model of the CO<sub>2</sub> breakthrough on the nano-sized K-CHA was found

394 to have 1–2 orders of magnitude higher  $k_{LDF}$  compared to that of the micron-sized K-CHA  
 395 (Table 3), consistent with the sharper experimental breakthrough curves. The calculated CO<sub>2</sub>  
 396 equilibrium loadings from the breakthrough curve modelling agree well with the  
 397 experimental values, within 10% error. The  $k_{LDF}$  for CO<sub>2</sub> of the micron-sized K-CHA are of a  
 398 similar magnitude to those of other commercial zeolite adsorbents such as NaX, CaA and  
 399 4A.[44, 57, 58] Modelling of the CO<sub>2</sub> breakthrough curves for the micron-sized K-CHA  
 400 using the maximal loading term extracted from the isotherm modelling resulted in slight  
 401 offsets between the experimental and modelled curves. This is may be due to the CO<sub>2</sub>  
 402 equilibrium adsorption curves of the micron-sized K-CHA having not completely levelled off  
 403 leading to an overestimation of the  $q_{max,i}$ . [59] To fit the model to the experimental data the  
 404 maximal loading terms were reduced by 10%, 7% and 4% for the curves at 20 °C, 40 °C and  
 405 60 °C respectively. The adjustments to the maximal loading did not affect the  $k_{LDF}$  values of  
 406 the fitted curves (Fig. S12).[60]

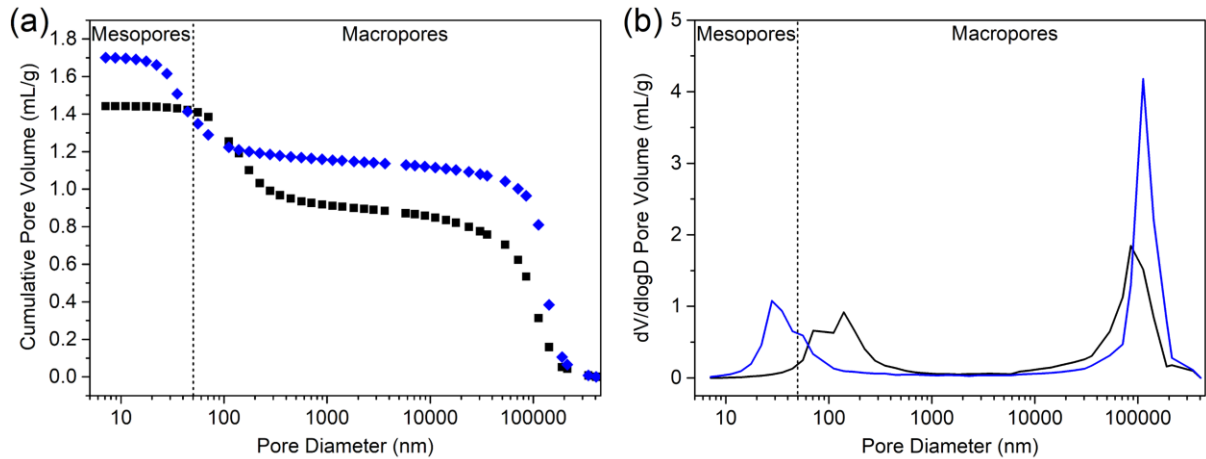


407  
 408 **Figure 3.** Experimental CO<sub>2</sub> breakthrough curves (black squares) and the fitted model of CO<sub>2</sub>  
 409 breakthrough curves (red lines) using the parameters from Tables 1 and S4 for the micron-  
 410 sized K-CHA at (a) 20 °C, (b) 40 °C and (c) 60 °C, and for the nano-sized K-CHA at (d) 20  
 411 °C, (e) 40 °C and (f) 60 °C.

412 **Table 3.** Calculated linear driving force parameters and CO<sub>2</sub> equilibrium loadings obtained  
 413 from the modelling of the CO<sub>2</sub> breakthrough curves for the nano- and micron-sized K-CHA  
 414 at 20, 40 and 60 °C.

Temperature (°C)	$k_{LDF}$ (s <sup>-1</sup> )		CO <sub>2</sub> equilibrium loading (mmol/g)	
	Nano-sized K- CHA	Micron-sized K-CHA	Nano-sized K- CHA	Micron-sized K-CHA
20	2.37	0.0221	2.35	2.26
40	2.93	0.0442	1.61	1.51
60	3.27	0.125	0.92	0.90

415 To better understand the effect of particle size on the performance and diffusion properties of  
 416 the K-CHA samples, mercury porosimetry analysis of the meshed K-CHA samples was  
 417 performed, and diffusion resistances were considered using established correlations in the  
 418 literature.[46, 61] Plots of the pore diameter against the cumulative pore volume (Fig. 4a) and  
 419 pore size distribution (Fig. 4b) of the meshed K-CHA samples reveal two intrusion events  
 420 corresponding to the initial filling of the macropores (interparticle porosity) and the filling of  
 421 the remaining macropores and mesopores. Both samples exhibit similar intrusion of the  
 422 interparticle porosity, however, the distribution of the macropores is different. The majority  
 423 (80%) of the macropore volume of the meshed nano-sized K-CHA occurs for pores  $\geq 6 \mu\text{m}$   
 424 while for the meshed micron-sized K-CHA this corresponds to 61% (Table S7). This may be  
 425 ascribed to the more uniform morphology of the nano-sized K-CHA compared to the flake-  
 426 like morphology of the micron-sized K-CHA. The filling of the mesopores (7–50 nm) shows  
 427 that the meshed nano-sized K-CHA exhibits  $\approx 14$  times higher mesopore volume compared to  
 428 the meshed micron-sized K-CHA. This is a clear result of the meshed particle being  
 429 composed of smaller discrete nanocrystals. For the nano-sized K-CHA the mesopores  
 430 account for approximately 17% of the total pore volume determined by Hg porosimetry,  
 431 while for the micron-sized K-CHA this value is 1.3%.



432  
 433 **Figure 4.** Plot of the pore diameter (nm) vs the (a) cumulative pore volume, and (b) pore size  
 434 distribution for the meshed nano-sized (blue) and micron-sized (black) K-CHA zeolite.  
 435

436 Considering that each of the eight-membered ring pore apertures of K-CHA are occupied by  
 437 extra-framework  $K^+$  cations and are comparable in size to  $CO_2$ , like for 4A zeolite, it may be  
 438 expected that the diffusion behaviour of K-CHA to be micropore controlled.[62] However,  
 439 considering that the meshed particle sizes are 0.25–0.5 mm, axial dispersion may be expected  
 440 to contribute significantly to the mass transfer behaviour.[63] Recent breakthrough curve  
 441 analysis of  $N_2/O_2$  on lithium exchanged low silica X (LiLSX) zeolite demonstrated that axial  
 442 dispersion effects must be considered for small particles and at low Reynolds number which  
 443 is the case in this work.[64] The contributions from the different diffusion resistances to the  
 444 overall mass transfer coefficient  $k_i$  were calculated using equation (14), which is a  
 445 generalisation of the Glueckauf approximation[46]:

446

$$\frac{1}{k_i} = \frac{Kr_p}{3k_f} + \frac{Kr_p^2}{15\varepsilon_p D_p} + \frac{r_c^2}{15D_c} \quad (14)$$

447 where the first, second and third terms on the right-hand side of equation 14 represent the  
 448 film mass transfer, macropore, and micropore resistances, and  $K$  is the equilibrium Henry's  
 449 law constant. Calculation of the values for the axial dispersion, film and macropore  
 450 contributions were performed using established correlations and experimental data.[46, 61]

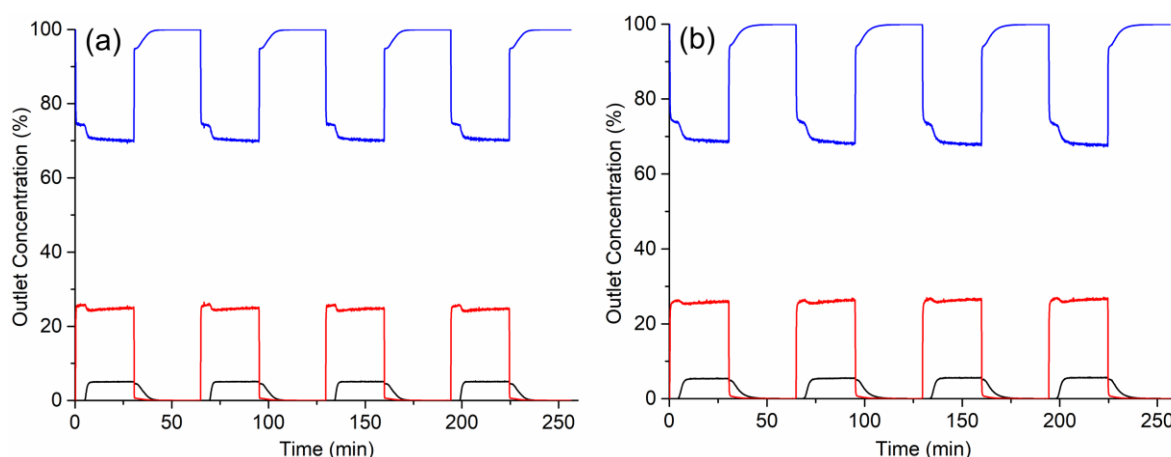
451 However, due to the unavailability of experimental intracrystalline diffusivity values for CO<sub>2</sub>  
452 in high-aluminium cation-containing chabazite zeolites, the micropore contribution was  
453 estimated by subtracting the film and macropore contributions from the effective mass  
454 transfer coefficients extracted from the breakthrough curve modelling. The calculated  
455 intracrystalline diffusivity values of CO<sub>2</sub> for the K-CHA zeolites are 3–4 orders of magnitude  
456 greater than for 4A.[65] Details describing the calculation of each contribution are provided  
457 in the supporting information; the values and percentages of  $k_i$  are presented in Tables S12–  
458 14. The calculations reveal that between the film, macropore and micropore resistances, the  
459 micropore contribution is the most significant, being several orders of magnitude greater and  
460 accounting for >99.5% of the mass transfer coefficient for the micron-sized K-CHA across all  
461 measured temperatures. For the nano-sized K-CHA the micropore resistance is much less  
462 significant than for the micron-sized K-CHA, but still accounts for 83, 87 and 92% of the  
463 mass transfer coefficient at 20, 40 and 60 °C respectively. Both samples exhibit similar  
464 absolute values of film and macropore resistance; their relative contribution is more  
465 significant for the nano-sized K-CHA. Both K-CHA samples exhibit similar absolute values  
466 for the contribution of axial dispersion, which are similar or greater in value to the  
467 contribution of the micropore resistance. For the micron-sized K-CHA, the ratio of the axial  
468 dispersion to micropore resistance increases from 0.8 at 20 °C to 1.1 at 40 °C and 2.1 at 60  
469 °C due to the greater decrease in the micropore resistance. For the nano-sized K-CHA, the  
470 ratio of the axial dispersion to the micropore resistance is significantly higher (54–91). This  
471 indicates that the mass transfer behaviour of the meshed nano-sized K-CHA is primarily  
472 affected by axial dispersion; the ratio of the axial dispersion to the micropore resistance  
473 decreases with increasing temperature.

474 For comparison, the contributions from the lumped resistances and axial dispersion were also  
475 explored by varying either the  $k_{LDF}$  parameter or axial dispersion values for the modelling of

476 the breakthrough curves.[58] Consistent with the trend of the calculated values presented in  
477 Table S12 the shape of the modelled CO<sub>2</sub> breakthrough curves for the nano-sized K-CHA are  
478 susceptible to variations in the axial dispersion, while varying the  $k_{LDF}$  parameter results in  
479 little change (Fig S13). In comparison, the micron-sized K-CHA is much more susceptible to  
480 changes of the  $k_{LDF}$  parameter, and similarly susceptible to changes of the axial dispersion  
481 (Fig. S14). While increased axial dispersion increases spreading of the MTZ, the  
482 experimental results presented here indicate that for adsorbent particles of identical size and  
483 composition, reducing the size of the discrete crystals within the meshed particle may reduce  
484 the size of the MTZ. Analysis of the results indicate this is primarily attributed to the  
485 reduction of the micropore resistance, which may be a consequence of the shorter  
486 intracrystalline diffusion pathway of CO<sub>2</sub> within the nano-sized K-CHA. While the  
487 introduction of mesoporosity has shown to improve the CO<sub>2</sub> adsorption kinetics for LTA  
488 zeolite, in the present case where the nano-sized K-CHA exhibits an order of magnitude  
489 greater mesopore volume than the micron-sized K-CHA, the contribution from the macropore  
490 diffusion resistance is negligible.[66]

491 Multiple cycles of CO<sub>2</sub> breakthrough, and desorption under pure He at 60 °C also  
492 demonstrates the improved performance of the nano-sized K-CHA (Fig. 5) which exhibits a  
493 29% higher CO<sub>2</sub> differential loading for the first cycle (Table 4). The CO<sub>2</sub> loading was  
494 calculated up to the first point of breakthrough. Upon subsequent cycles of CO<sub>2</sub> adsorption,  
495 and desorption under pure He, the CO<sub>2</sub> capacities of both samples decreases due to the  
496 formation of chemisorbed carbonate species and the incomplete removal of adsorbed CO<sub>2</sub> by  
497 He during the desorption step.[43] This is supported by integration of the CO<sub>2</sub> desorption  
498 curves for the nano and micron-sized K-CHA at 60 °C which afforded 0.76 and 0.73 mmol/g,  
499 or 87 and 88% of the differential loadings at saturation (Table 2). Over the next three cycles,  
500 on average, the nano-sized K-CHA exhibits better performance up to the end of pure

501 production of the weakly adsorbing component, losing only 14% of its initial CO<sub>2</sub> capacity  
 502 while the micron-sized K-CHA loses approximately 29% (Table 4). This may be due to  
 503 compositional inhomogeneity of the micron-sized K-CHA particles due to their preparation  
 504 by interzeolite conversion and the different solubilities of Si and Al species, as well as the  
 505 possibility of internal structural rearrangements due to the long hydrothermal treatment time  
 506 (15 days).[67] This rationale is supported by comparing the relative amounts of CO<sub>2</sub>  
 507 chemisorbed species. *In situ* FTIR spectroscopic analysis of the micron-sized K-CHA in the  
 508 presence of CO<sub>2</sub> (17.9 kPa) revealed ~3 times greater the amount of CO<sub>2</sub> chemisorbed  
 509 species compared to nano-sized K-CHA, *i.e.* 5% vs 1.7% of the total physisorbed and  
 510 chemisorbed CO<sub>2</sub> (Fig. S15).[43]



511  
 512 **Figure 5.** Four consecutive cycles of the adsorption step (He/N<sub>2</sub>/CO<sub>2</sub>, 70/25/5) and  
 513 desorption step (He, 100) for breakthrough curve analysis on the (a) nano-sized K-CHA and  
 514 (b) micron-sized K-CHA at 60 °C. Colour legend: He (blue), N<sub>2</sub> (red), and CO<sub>2</sub> (black).

515 **Table 4.** Differential loading of CO<sub>2</sub> calculated from CO<sub>2</sub> breakthrough curves at  $C/C_0 >$   
 516  $1 \times 10^{-4}$  on nano- and micron-sized K-CHA subjected to multiple cycles of breakthrough  
 517 (He/N<sub>2</sub>/CO<sub>2</sub>, 70/25/5) and desorption (He, 100) at 60 °C.

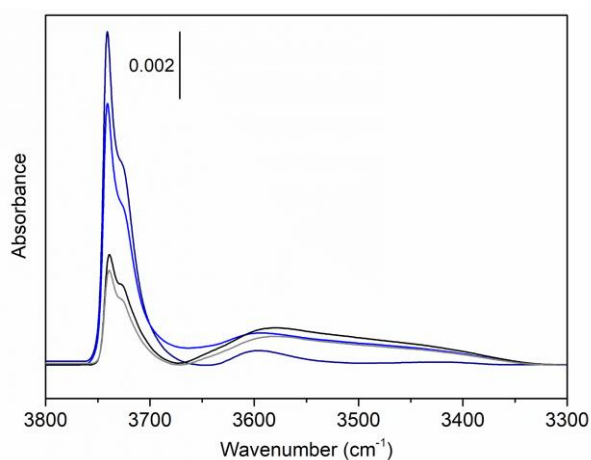
Cycle	CO <sub>2</sub> differential loading, q (mmol/g)	
	Nano-sized K- CHA	Micron-sized K-CHA
1	0.66	0.51
2	0.56	0.35
3	0.56	0.36
4	0.57	0.36

518

## 519 ***In situ* FTIR Analysis of the Silanol Environments**

520 To consider the role defects may play in the separation performance of the K-CHA samples,  
521 *in situ* FTIR spectroscopic analysis was also employed to examine the distributions of silanol  
522 environments on both K-CHA samples (Fig. 6). Analysis before and after breakthrough curve  
523 experiments reveals two peaks at  $3740\text{ cm}^{-1}$  and  $3727\text{ cm}^{-1}$  attributed to isolated silanol sites  
524 corresponding to the external surfaces of the different K-CHA samples.[68] These peaks are  
525 significantly more intense for the nano-sized K-CHA due to its larger external surface area.  
526 Both micron and nano-sized K-CHA samples show a broad complex band in the range of  
527  $3333$  and  $3668\text{ cm}^{-1}$ . These peaks can be attributed to the internal silanol sites exhibiting  
528 strong hydrogen bonding between them.[68] The micron-sized K-CHA exhibits a greater  
529 initial population (black trace) of strong internal hydrogen bonding sites which may reflect  
530 internal framework T-atom vacancies or missing T–O–T bonds due to the intergrown nature  
531 of the crystallites. After multiple pre-treatment and breakthrough cycles this band decreases  
532 slightly (grey trace). Conversely, the nano-sized K-CHA exhibits fewer sites initially (navy  
533 trace) and an increased population of these sites after multiple pre-treatment and  
534 breakthrough cycles (blue trace). This suggests that despite an increase in the population of  
535 strong hydrogen-bonding silanol sites on the nano-sized K-CHA the diffusion performance is  
536 dominated by the effect of the particle size difference. Deconvolution and exact peak  
537 assignment in this region is not possible using exclusively FTIR spectroscopy and requires  
538 additional characterization techniques (*i.e.*  $^1\text{H}$  MAS NMR) beyond the scope of this work.  
539 Table 5 presents the concentration of the silanol sites obtained by integration of the silanol  
540 region for both the nano- and micron-sized K-CHA samples before and after the  
541 breakthrough measurements. For both the nano- and micron-sized K-CHA samples a  
542 reduction of  $\sim 27\%$  of the silanol sites are observed after the breakthrough measurements

543 (Table 5). This can be partly attributed to the residual chemisorbed species chemically  
 544 bonded to the silanol sites and in agreement with our previous work.[43]



545  
 546 **Figure 6.** *In situ* FTIR spectra at 25 °C highlighting the silanol region of the nano-sized  
 547 (navy, blue) and micron-sized (black, grey) K-CHA samples zeolite (before, after  
 548 breakthrough curve analysis). Samples were pre-treated at 300 °C under high vacuum ( $10^{-6}$   
 549 kPa) prior to measurement.

550  
 551  
 552 **Table 5.** The concentration of silanol sites of micron and nano-sized K-CHA samples before  
 553 (fresh) and after (used) breakthrough measurements obtained using *in situ* FTIR  
 554 spectroscopy.

Sample		Silanol site concentration ( $\text{cm}^{-1}\cdot\text{g}^{-1}$ )
Nano-sized K-CHA	Fresh	403
	Used	288
Micron-sized K-CHA	Fresh	306
	Used	224

555

## 556 Conclusions

557 As we move towards the need to control process rate, by improving the diffusion properties  
 558 of zeolites through the organic-template free direct synthesis of discrete zeolite nanoparticles,  
 559 instead of employing post-synthetic treatments, significant enhancements in the separation  
 560 performance can be achieved. By comparing meshed micron-sized and nano-sized K-CHA  
 561 with identical Si/Al ratios and cation compositions for  $\text{CO}_2$  separation from  $\text{N}_2$ , the diffusion  
 562 of  $\text{CO}_2$  through the bed of meshed nano-sized K-CHA is more rapid and uniform.

563 Breakthrough curve analysis shows steeper breakthrough curves and more rapid achievement  
564 of equilibrium for the meshed nano-sized K-CHA due to the smaller discrete particle size.  
565 While textural analysis by Hg porosimetry reveals improved mesoporosity for the nano-sized  
566 K-CHA, back-calculation of the diffusion coefficients reveals significantly lower micropore  
567 diffusion resistance as responsible for the improved mass transfer behaviour. This translates  
568 to a greater  $k_{LDF}$  of the modelled and fitted CO<sub>2</sub> breakthrough curves and a reduction in the  
569 size of the MTZ by 17% despite the significant contribution from axial dispersion to the mass  
570 transfer behaviour. Furthermore, we also observe that the nano-sized K-CHA has  
571 approximately three times less CO<sub>2</sub> chemisorbed species than micron-sized K-CHA. When  
572 scouting for improved adsorbents, most academic researchers often concentrate on capacity  
573 and selectivity and pay less attention to the kinetics of the process. The combination of these  
574 three features will determine the productivity, often referred to in catalysis as STY (space  
575 time yield, units: moles of a desired product.time<sup>-1</sup>·reactor volume<sup>-1</sup>). STY is a key parameter  
576 to design the size of a unit, *i.e.*, this investment cost (CAPEX). While these results support  
577 the potential of nanozeolites in realising greater performance improvements, further  
578 investigation of the diffusion behaviour of nanozeolites in larger columns and their  
579 comparison to micron-sized counterparts will yield greater insights due to the variety of pore  
580 sizes, framework topologies, elemental compositions and shaping factors of zeolites which  
581 influence the diffusion properties.

## 582 **Declaration of Competing Interests**

583 The authors declare no competing financial or professional interests.

## 584 **Acknowledgements**

585 E. B. C. would like to thank Carsten Blum and Sebastian Ehrling for their helpful  
586 discussions, and Izabel Medeiros-Costa for her help with mercury porosimetry. This project

587 has received funding from the Region of Normandy via the Label of Excellence for the  
588 Centre of Zeolites and Nanoporous Materials and the Industrial Chair Project “ECOGAS”  
589 supported by the Region of Normandy and TotalEnergies.

590

## 591 **References**

592

593 [1] S. Sircar, A.L. Myers, Gas Separation by Zeolites, in: S.M. Auerbach, K.A. Carrado, P.K.  
594 Dutta (Eds.) Handbook of Zeolite Science and Technology, Marcel Dekker, Inc., New York,  
595 Basel, 2003, pp. 1063-1104.

596 [2] Y.S. Bae, R.Q. Snurr, Development and evaluation of porous materials for carbon dioxide  
597 separation and capture, *Angew. Chem. Int. Ed.*, 50 (2011) 11586-11596.

598 [3] A. Samanta, A. Zhao, G.K. Shimizu, P. Sarkar, R. Gupta, Post-combustion CO<sub>2</sub> capture  
599 using solid sorbents: a review, *Ind. Eng. Chem. Res.*, 51 (2012) 1438-1463.

600 [4] B. Li, Y. Duan, D. Luebke, B. Morreale, Advances in CO<sub>2</sub> capture technology: A patent  
601 review, *Appl. Energy*, 102 (2013) 1439-1447.

602 [5] D.Y. Leung, G. Caramanna, M.M. Maroto-Valer, An overview of current status of carbon  
603 dioxide capture and storage technologies, *Renew. Sust. Energ. Rev.*, 39 (2014) 426-443.

604 [6] O. Cheung, N. Hedin, Zeolites and related sorbents with narrow pores for CO<sub>2</sub> separation  
605 from flue gas, *RSC Adv.*, 4 (2014) 14480-14494.

606 [7] M. Pera-Titus, Porous inorganic membranes for CO<sub>2</sub> capture: present and prospects,  
607 *Chem. Rev.*, 114 (2014) 1413-1492.

608 [8] P.A. Webley, Adsorption technology for CO<sub>2</sub> separation and capture: a perspective,  
609 *Adsorption*, 20 (2014) 225-231.

610 [9] N. Gargiulo, F. Pepe, D. Caputo, CO<sub>2</sub> adsorption by functionalized nanoporous materials:  
611 a review, *J. Nanosci. Nanotechnol.*, 14 (2014) 1811-1822.

612 [10] S.-Y. Lee, S.-J. Park, A review on solid adsorbents for carbon dioxide capture, *J. Ind.*  
613 *Eng. Chem.*, 23 (2015) 1-11.

614 [11] N. Kosinov, J. Gascon, F. Kapteijn, E.J. Hensen, Recent developments in zeolite  
615 membranes for gas separation, *J. Membr. Sci.*, 499 (2016) 65-79.

616 [12] E.S. Sanz-Perez, C.R. Murdock, S.A. Didas, C.W. Jones, Direct capture of CO<sub>2</sub> from  
617 ambient air, *Chem. Rev.*, 116 (2016) 11840-11876.

618 [13] M. Younas, M. Sohail, L. Leong, M. Bashir, S. Sumathi, Feasibility of CO<sub>2</sub> adsorption  
619 by solid adsorbents: a review on low-temperature systems, *Int. J. Environ. Sci. Technol.*, 13  
620 (2016) 1839-1860.

621 [14] H.A. Patel, J. Byun, C.T. Yavuz, Carbon dioxide capture adsorbents: chemistry and  
622 methods, *ChemSusChem*, 10 (2017) 1303-1317.

623 [15] M. Vinoba, M. Bhagiyalakshmi, Y. Alqaheem, A.A. Alomair, A. Pérez, M.S. Rana,  
624 Recent progress of fillers in mixed matrix membranes for CO<sub>2</sub> separation: A review, *Sep.*  
625 *Purif. Technol.*, 188 (2017) 431-450.

626 [16] M. Abu Ghaliya, Y. Dahman, Development and evaluation of zeolites and metal-organic  
627 frameworks for carbon dioxide separation and capture, *Energy Technol.*, 5 (2017) 356-372.

628 [17] M. Oschatz, M. Antonietti, A search for selectivity to enable CO<sub>2</sub> capture with porous  
629 adsorbents, *Energy Environ. Sci.*, 11 (2018) 57-70.

630 [18] Y. Han, Z. Zhang, Nanostructured membrane materials for CO<sub>2</sub> capture: a critical  
631 review, *J. Nanosci. Nanotechnol.*, 19 (2019) 3173-3179.

632 [19] S. Kumar, R. Srivastava, J. Koh, Utilization of zeolites as CO<sub>2</sub> capturing agents:  
633 Advances and future perspectives, *J. CO<sub>2</sub> Util.*, 41 (2020) 101251.

634 [20] S.C. Peter, B. Ray, S.R. Churipard, An overview of the materials and methodologies for  
635 CO<sub>2</sub> capture under humid conditions, *J. Mater. Chem. A*, 9 (2021) 26498-26527.

636 [21] A.H. Farmahini, S. Krishnamurthy, D. Friedrich, S. Brandani, L. Sarkisov, Performance-  
637 based screening of porous materials for carbon capture, *Chem. Rev.*, 121 (2021) 10666-  
638 10741.

639 [22] R.S. Liu, X.D. Shi, C.T. Wang, Y.Z. Gao, S. Xu, G.P. Hao, S. Chen, A.H. Lu, Advances  
640 in post- combustion CO<sub>2</sub> capture by physical adsorption: from materials innovation to  
641 separation practice, *ChemSusChem*, 14 (2021) 1428-1471.

642 [23] F.G. Kerry, *Industrial Gas Handbook: Gas Separation and Purification*, CRC press, Boca  
643 Raton, FL, 2007.

644 [24] Z. Zhang, T.N. Borhani, A.G. Olabi, Status and perspective of CO<sub>2</sub> absorption process,  
645 *Energy*, 205 (2020) 118057.

646 [25] F. Raganati, F. Miccio, P. Ammendola, Adsorption of carbon dioxide for post-  
647 combustion capture: a review, *Energy Fuels*, 35 (2021) 12845-12868.

648 [26] R.L. Siegelman, E.J. Kim, J.R. Long, Porous materials for carbon dioxide separations,  
649 *Nat. Mater.*, 20 (2021) 1060-1072.

650 [27] P. Hovington, O. Ghaffari-Nik, L. Mariac, A. Liu, B. Henkel, S. Marx, Rapid cycle  
651 temperature swing adsorption process using solid structured sorbent for CO<sub>2</sub> capture from  
652 cement flue gas, *Proceedings of the 15th Greenhouse Gas Control Technologies Conference*,  
653 Abu Dhabi, UAE, 2021, pp. 15-18.

654 [28] W. Vermeiren, J.-P. Gilson, Impact of Zeolites on the Petroleum and Petrochemical  
655 Industry, *Top. Catal.*, 52 (2009) 1131-1161.

656 [29] P. Peng, D. Stosic, X.-M. Liu, Z.-F. Yan, S. Mintova, Strategy towards enhanced  
657 performance of zeolite catalysts: raising effective diffusion coefficient versus reducing  
658 diffusion length, *Chem. Eng. J.*, 385 (2020) 123800.

659 [30] P. Peng, D. Stosic, A. Aitblal, A. Vimont, P. Bazin, X.-M. Liu, Z.-F. Yan, S. Mintova,  
660 A. Travert, Unraveling the diffusion properties of zeolite-based multicomponent catalyst by  
661 combined gravimetric analysis and IR spectroscopy (AGIR), *ACS Catal.*, 10 (2020) 6822-  
662 6830.

663 [31] D. Kerstens, B. Smeyers, J. Van Waeyenberg, Q. Zhang, J. Yu, B.F. Sels, State of the art  
664 and perspectives of hierarchical zeolites: practical overview of synthesis methods and use in  
665 catalysis, *Adv. Mater.*, 32 (2020) 2004690.

666 [32] E.-P. Ng, D. Chateigner, T. Bein, V. Valtchev, S. Mintova, Capturing ultrasmall EMT  
667 zeolite from template-free systems, *Science*, 335 (2012) 70-73.

668 [33] H. Awala, J.-P. Gilson, R. Retoux, P. Boullay, J.-M. Goupil, V. Valtchev, S. Mintova,  
669 Template-free nanosized faujasite-type zeolites, *Nat. Mater.*, 14 (2015) 447-451.

670 [34] J. Grand, N. Barrier, M. Debost, E.B. Clatworthy, F. Laine, P. Boullay, N. Nesterenko,  
671 J.-P. Dath, J.-P. Gilson, S. Mintova, Flexible Template-Free RHO Nanosized Zeolite for  
672 Selective CO<sub>2</sub> Adsorption, *Chem. Mater.*, 32 (2020) 5985-5993.

673 [35] M. Debost, P.B. Klar, N. Barrier, E.B. Clatworthy, J. Grand, F. Lainé, P. Brazda, L.  
674 Palatinus, N. Nesterenko, P. Boullay, S. Mintova, Synthesis of discrete CHA zeolite  
675 nanocrystals without organic templates for selective CO<sub>2</sub> capture, *Angew. Chem. Int. Ed.*, 59  
676 (2020) 23491-23495.

677 [36] E.B. Clatworthy, M. Debost, N. Barrier, S.p. Gascoin, P. Boullay, A.I. Vicente, J.-P.  
678 Gilson, J.-P. Dath, N. Nesterenko, S. Mintova, Room-Temperature Synthesis of BPH Zeolite  
679 Nanosheets Free of Organic Template with Enhanced Stability for Gas Separations, *ACS*  
680 *Appl. Nano Mater*, 4 (2020) 24-28.

681 [37] E.B. Clatworthy, A.A. Paecklar, E. Dib, M. Debost, N. Barrier, P. Boullay, J.-P. Gilson,  
682 N. Nesterenko, S. Mintova, Engineering RHO Nanozeolite: Controlling the Particle  
683 Morphology, Al and Cation Content, Stability, and Flexibility, *ACS Appl. Energy Mater.*, 5  
684 (2022) 6032-6042.

685 [38] M. Debost, E.B. Clatworthy, J. Grand, N. Barrier, N. Nesterenko, J.-P. Gilson, P.  
686 Boullay, S. Mintova, Direct synthesis of nanosized CHA zeolite free of organic template by a  
687 combination of cations as structure directing agents, *Microporous Mesoporous Mater.*, (2022)  
688 112337.

689 [39] K.C. Omehia, A.G. Clements, S. Michailos, K.J. Hughes, D.B. Ingham, M.  
690 Pourkashanian, Techno- economic assessment on the fuel flexibility of a commercial scale  
691 combined cycle gas turbine integrated with a CO<sub>2</sub> capture plant, *Int. J. Energy Res.*, 44  
692 (2020) 9127-9140.

693 [40] J. Shang, G. Li, R. Singh, Q. Gu, K.M. Nairn, T.J. Bastow, N. Medhekar, C.M. Doherty,  
694 A.J. Hill, J.Z. Liu, P.A. Webley, Discriminative separation of gases by a “molecular  
695 trapdoor” mechanism in chabazite zeolites, *J. Am. Chem. Soc.*, 134 (2012) 19246-19253.

696 [41] F.N. Ridha, P.A. Webley, Anomalous Henry's law behavior of nitrogen and carbon  
697 dioxide adsorption on alkali-exchanged chabazite zeolites, *Sep. Purif. Technol.*, 67 (2009)  
698 336-343.

699 [42] S. Ghojavand, E.B. Clatworthy, A. Vicente, E. Dib, V. Ruaux, M. Debost, J. El Fallah,  
700 S. Mintova, The role of mixed alkali metal cations on the formation of nanosized CHA  
701 zeolite from colloidal precursor suspension, *J. Colloid Interface Sci.*, 604 (2021) 350-357.

702 [43] S. Ghojavand, B. Coasne, E.B. Clatworthy, R. Guillet-Nicolas, P. Bazin, M. Desmurs, L.  
703 Jacobo Aguilera, V. Ruaux, S. Mintova, Alkali Metal Cations Influence the CO<sub>2</sub> Adsorption  
704 Capacity of Nanosized Chabazite: Modeling vs Experiment, *ACS Appl. Nano Mater.*, 5  
705 (2022) 5578-5588.

706 [44] A. Möller, R. Eschrich, C. Reichenbach, J. Guderian, M. Lange, J. Möllmer, Dynamic  
707 and equilibrium-based investigations of CO<sub>2</sub>-removal from CH<sub>4</sub>-rich gas mixtures on  
708 microporous adsorbents, *Adsorption*, 23 (2017) 197-209.

709 [45] N.S. Wilkins, A. Rajendran, Measurement of competitive CO<sub>2</sub> and N<sub>2</sub> adsorption on  
710 Zeolite 13X for post-combustion CO<sub>2</sub> capture, *Adsorption*, 25 (2019) 115-133.

711 [46] D.M. Ruthven, *Principles of Adsorption and Adsorption Processes*, Wiley, New York,  
712 1984.

713 [47] W. Kast, *Adsorption aus der Gasphase. Ingenieurwissenschaftliche Grundlagen und*  
714 *technische Verfahren*, VCH, Weinheim, Germany, 1988.

715 [48] D.B. Bathen, M, *Adsorptionstechnik*, Springer, Berlin, 2001.

716 [49] E. Glueckauf, Theory of chromatography. Part 10.—Formulæ for diffusion into spheres  
717 and their application to chromatography, *Trans. Faraday Society*, 51 (1955) 1540-1551.

718 [50] A. Findikakis, Heat Capacity Analysis Report, Yucca Mountain Project, Las Vegas, NV  
719 (United States)2004.

720 [51] M. Bourgogne, J.-L. Guth, R. Wey, Process for the preparation of synthetic zeolites, and  
721 zeolites obtained by said process, *Compagnie Francaise de Raffinage*1985.

722 [52] S.-H. Hong, M.-S. Jang, S.J. Cho, W.-S. Ahn, Chabazite and zeolite 13X for CO<sub>2</sub>  
723 capture under high pressure and moderate temperature conditions, *Chem. Commun.*, 50  
724 (2014) 4927-4930.

725 [53] M. Calligaris, G. Nardin, L. Randaccio, Cation site location in hydrated chabazites.  
726 Crystal structure of potassium-and silver-exchanged chabazites, *Zeolites*, 3 (1983) 205-208.

727 [54] J. Zhang, R. Singh, P.A. Webley, Alkali and alkaline-earth cation exchanged chabazite  
728 zeolites for adsorption based CO<sub>2</sub> capture, *Microporous Mesoporous Mater.*, 111 (2008) 478-  
729 487.

- 730 [55] T.D. Pham, M.R. Hudson, C.M. Brown, R.F. Lobo, Molecular basis for the high CO<sub>2</sub>  
731 adsorption capacity of chabazite zeolites, *ChemSusChem*, 7 (2014) 3031-3038.
- 732 [56] T. Du, X. Fang, L. Liu, J. Shang, B. Zhang, Y. Wei, H. Gong, S. Rahman, E.F. May,  
733 P.A. Webley, An optimal trapdoor zeolite for exclusive admission of CO<sub>2</sub> at industrial carbon  
734 capture operating temperatures, *Chem. Commun.*, 54 (2018) 3134-3137.
- 735 [57] H. Yi, H. Deng, X. Tang, Q. Yu, X. Zhou, H. Liu, Adsorption equilibrium and kinetics  
736 for SO<sub>2</sub>, NO, CO<sub>2</sub> on zeolites FAU and LTA, *J. Hazard. Mater.*, 203 (2012) 111-117.
- 737 [58] L.F. Zafanelli, A. Henrique, M. Karimi, A.E. Rodrigues, J.A. Silva, Single- and  
738 Multicomponent Fixed Bed Adsorption of CO<sub>2</sub>, CH<sub>4</sub>, and N<sub>2</sub> in Binder-Free Beads of 4A  
739 Zeolite, *Ind. Eng. Chem. Res.*, 59 (2020) 13724-13734.
- 740 [59] Q.H. Dirar, K.F. Loughlin, Intrinsic adsorption properties of CO<sub>2</sub> on 5A and 13X zeolite,  
741 *Adsorption*, 19 (2013) 1149-1163.
- 742 [60] J.C. Knox, A.D. Ebner, M.D. LeVan, R.F. Coker, J.A. Ritter, Limitations of  
743 breakthrough curve analysis in fixed-bed adsorption, *Ind. Eng. Chem. Res.*, 55 (2016) 4734-  
744 4748.
- 745 [61] N.S. Wilkins, A. Rajendran, S. Farooq, Dynamic column breakthrough experiments for  
746 measurement of adsorption equilibrium and kinetics, *Adsorption*, 27 (2021) 397-422.
- 747 [62] D.M. Ruthven, Diffusion in type A zeolites: New insights from old data, *Microporous*  
748 *Mesoporous Mater.*, 162 (2012) 69-79.
- 749 [63] M. Suzuki, J. Smith, Axial dispersion in beds of small particles, *The Chemical*  
750 *Engineering Journal*, 3 (1972) 256-264.
- 751 [64] A. Moran, M. Patel, O. Talu, Axial dispersion effects with small diameter adsorbent  
752 particles, *Adsorption*, 24 (2018) 333-344.
- 753 [65] H. Yucel, D.M. Ruthven, Diffusion of CO<sub>2</sub> in 4A and 5A zeolite crystals, *J. Colloid*  
754 *Interface Sci.*, 74 (1980) 186-195.
- 755 [66] C. Chen, W.-S. Ahn, CO<sub>2</sub> adsorption on LTA zeolites: Effect of mesoporosity, *Appl.*  
756 *Surf. Sci.*, 311 (2014) 107-109.
- 757 [67] J. Devos, M.A. Shah, M. Dusselier, On the key role of aluminium and other heteroatoms  
758 during interzeolite conversion synthesis, *RSC Adv.*, 11 (2021) 26188-26210.
- 759 [68] E. Dib, I.M. Costa, G.N. Vayssilov, H.A. Aleksandrov, S. Mintova, Complex H-bonded  
760 silanol network in zeolites revealed by IR and NMR spectroscopy combined with DFT  
761 calculations, *J. Mater. Chem. A*, 9 (2021) 27347-27352.